The Electrochemical Society
Advancing solid state & electrochemical science & technology

The Early-Stage Corrosion of Copper Materials in Chloride and Sulfide Solutions: Nanoscale Characterization and The Effect of Microstructure

View the article online for updates and enhancements.

The Early-Stage Corrosion of Copper Materials in Chloride and Sulfide Solutions: Nanoscale Characterization and The Effect of Microstructure

Mengnan Guo,[1,*,a,z] Kevin Daub,[1] Qingshan Dong,[1] Fei Long,[1] W. Jeffrey Binns,[2] Mark R. Daymond,[1] David W. Shoesmith,[3,**] James J. Noël,[3,***] and Suraj Y. Persaud[1,z]

[1]*Department of Mechanical and Materials Engineering, Queen's University, Kingston, ON K7L 3N6, Canada*
[2]*Nuclear Waste Management Organization, Toronto, ON M4T 2S3, Canada*
[3]*Department of Chemistry, University of Western Ontario, London, ON N6A 3K7, Canada*

The microstructures of copper (Cu) materials were investigated by electron backscatter diffraction, showing that electrodeposited (ED) Cu has a homogenous polycrystalline microstructure, while cold spray (CS) Cu has a heterogeneous microstructure with varying grain size, pores, and interfacial splat regions. The corrosion rate was examined by corrosion potential (E_{CORR}) and polarization resistance (R_p) measurements on Cu specimens in solutions containing 0.1 M NaCl + 1×10^{-3} M Na$_2$S. Although the as sprayed CS-Cu was the least corrosion resistant, the corrosion rate of the heat-treated CS-Cu was similar to that of the ED-Cu and wrought Cu (SKB-Cu). Electrochemical behaviours of Cu materials were investigated by either a potentiodynamic scan or a potentiostatic polarization at a more positive potential ($E > E_{CORR}$) for various experiment durations up to 4 h, showing that the heat-treated CS-Cu, SKB-Cu and ED-Cu exhibited very similar behaviour while the as sprayed CS-Cu showed erratic behavior consistent with a variable surface reactivity. Nanoscale scanning transmission electron microscopy analysis has been performed at the cross-section of an anodically-oxidized CS-Cu specimen, revealing a two-layer film structure, mostly composed of Cu sulfide, with a minor diffusion of sulfur in the local area of an interfacial splat boundary tip.

The safe and permanent disposal of high-level nuclear waste is critical if nuclear power is to remain a viable energy source. The accepted method in many countries, including Canada, Sweden, and Finland, is the burial of used nuclear fuel in a deep geological repository (DGR), consisting of multiple natural and engineered barriers to isolate the nuclear waste from the environment.[1–4] In particular, the proposed disposal plan in Canada developed by the Nuclear Waste Management Organization (NWMO), involves the encapsulation of used fuels in a used fuel container (UFC), surrounded by a highly-compacted bentonite buffer box safely emplaced at a depth ⩾500 m in a DGR.[1,5] A key engineered component in the DGR design is the UFC, comprising a carbon steel vessel (ASME SA516 Gr.70) with an approximately 3 mm-thick Cu coating, applied via electrodeposition and cold spray deposition technologies, acting as the corrosion barrier.[6,7] The choice of Cu as the corrosion-resistant material was initially based on the element's thermodynamic stability under anticipated anoxic DGR conditions, justified by archaeological studies and the existence of naturally occurring copper metals that have remained intact in the subterranean environment for millions/billions of years.[1,8–10] A comprehensive description of current UFC designs can be found elsewhere,[6,7,11,12] including detailed discussions on coating deposition technologies, the current conservative Cu corrosion allowance, and manufacturing considerations.

Once the UFC is emplaced, the specific corrosion processes governing container degradation will change as the DGR conditions evolve over its lifetime (i.e., 1 million years).[1,2,13] The DGR conditions will evolve from initially warm, humid, and oxidizing to eventually cool, dry, and anoxic as the fuel decays, heat production decreases, and the O$_2$ trapped upon emplacement is rapidly depleted by microbial, mineral and minor container corrosion reactions.[2] Notably, the specific period required for the

evolution of redox conditions in a DGR remains uncertain and significantly variable. Recent full-scale underground field studies suggest that anaerobic conditions are reached within a few weeks to a few months[14] while other authors report that O$_2$ may be consumed within the first 10 to 100 years after the burial of containers in the DGR.[15] Regardless, the vast majority of the lifetime of the DGR will exist in an anerobic condition. Without oxygen, sulfide-induced Cu corrosion will become the dominant reaction, since Cu becomes unstable when exposed to sulfide (as SH$^-$).[16–19] Potential sources of dissolved sulfide in a DGR are the dissolution of sulfide minerals, such as pyrite (FeS$_2$) in the rock, and, more importantly, remotely produced SH$^-$, generated from SO$_4$$^{2-}$ via the action of anaerobic sulfate-reducing bacteria (SRB). Consequently, if dissolved sulfide is present in the proximity of the container under anoxic DGR conditions, sulfidation of Cu will be initiated via reaction (1).

$$2 \text{ Cu}_{(s)} + \text{SH}^-_{(aq)} + \text{H}_2\text{O}_{(l)} \rightarrow \text{Cu}_2\text{S}_{(s)} + \text{H}_{2(g)} + \text{OH}^-_{(aq)} \quad [1]$$
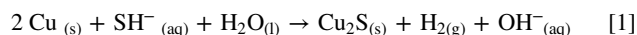
Numerous corrosion studies have been performed on SKB phosphorus-doped oxygen-free wrought Cu (a reference material, supplied by the Swedish Nuclear Waste Management Organization), demonstrating that sulfide-induced Cu corrosion is driven by the formation of chalcocite (Cu$_2$S) films on the Cu surface.[16–21] Chen et al.[20,21] showed that film structure and growth kinetics were determined by the balance between SH$^-$ transport from bulk solution to the Cu surface and the interfacial reaction rate with SH$^-$, and the competition for surface adsorption sites between SH$^-$ and chloride (Cl$^-$), with Cl$^-$ being the dominant groundwater anion.[22] It has also been shown that while the film growth kinetics may change, the Cu$_2$S film is commonly porous and only partially protective. Since the interfacial reaction rate is anticipated to be rapid compared to the slow transport of SH$^-$ from remote locations to the UFC surface through the compacted bentonite clay, corrosion would be expected to propagate uniformly with the formation of porous films on Cu.[23,24]

Film growth was found to depend on three critical parameters:[16,17] (i) the concentrations of sulfide ([SH$^-$]) and chloride ([Cl$^-$]); (ii) the ratio between [SH$^-$] and [Cl$^-$]; and (iii) the flux of SH$^-$ to the Cu surface, which determines whether a

porous or a partially protective sulfide film would form on Cu. Sulfide concentrations are expected to be below 10^{-4} M in Swedish and Finnish DGRs,[4] and $<10^{-6}$ M in a Canadian DGR.[2] Due to the anticipated low [SH$^-$] and the extremely low flux of SH$^-$ through the compacted clay, a very low [SH$^-$] would be established on the UFC surface, making the possibility of passive sulfide film formation unlikely, leading to an extremely low probability for localized corrosion. Martino et al.[19,25,26] showed that electrochemically-grown sulfide films exhibited similar dependencies on [SH$^-$], [Cl$^-$], their ratio, and the transport of [SH$^-$]. Their goal was to determine the probability of passive film formation on Cu, and, equally importantly, to determine whether the properties of the anodically grown films were similar to those formed under natural corrosion conditions. It was claimed that the film growth mechanisms were similar under both corrosion and electrochemical conditions,[26] and that the formation of passive sulfide films would only be possible when a high SH$^-$ flux was coupled with a high [SH$^-$]. Such a condition is not expected in the vicinity of the UFCs in a Canadian DGR.

Prior studies have provided valuable information on the mechanism of film growth under various aqueous solution conditions, such as at various [SH$^-$] and/or [Cl$^-$] and various SH$^-$ fluxes, and at different buffered conditions, with the addition of anions that are relevant to the groundwaters in a DGR.[16,17,20,22,26–29] However, they have not elucidated the influence of microstructural changes brought on by different Cu coating procedures (e.g., electrodeposited, and cold sprayed Cu) in the aqueous sulfide and chloride solutions. In addition, the microstructural variations among different Cu materials, such as the presence of local pores/cavities, residual stress/high dislocation density and crystallographic texture, may exert significant influences on the location where corrosion initiates and then propagates. The location of corrosion is often controlled by metallurgical factors, and a heterogeneous microstructure can change the kinetic parameters of corrosion propagation, for example by exerting an effect on diffusion and electrochemical polarization.[30–32] The microstructure-corrosion relationship remains to be addressed for Cu coatings in UFC applications under anoxic sulfide-induced corrosion conditions. Although microstructural characterizations of Cu coatings materials for UFCs were performed by Yu et al.[33] and Li et al.,[34] providing implications associated with

UFC corrosion in terms of material grain size, grain boundary character and crystallographic texture, no direct evidence was reported based on any data obtained from electrochemical and corrosion techniques.

In this paper, the early-stage corrosion of a variety of Cu materials is studied in aqueous sulfide and chloride containing solutions. The primary goal is to investigate the influence of microstructure, in particular defects, with an emphasis on the effect of splat interfaces (in cold-sprayed specimens), crystallographic orientation, and grain boundary character, on the corrosion of Cu materials. SEM/EBSD analysis was performed before corrosion and electrochemical experiments, providing crystallographic texture information. This microscale analysis is complemented with nanoscale characterization, specifically by STEM-EDX. When combined with electrochemical measurements, this multi-scale characterization yields an understanding of the distribution of corrosion damage, the associated mechanism, and, importantly, the local nanoscale chemistry changes at particular interfaces/boundaries on a corroded Cu-coated specimen, with the potential for sulfide penetration a specific focus for the latter.

Experimental

Materials.—Various Cu materials were investigated: P-doped O-free wrought Cu (SKB-Cu), electrodeposited Cu (ED-Cu), as-sprayed cold spray deposited Cu (AS-CS-Cu) and heat-treated cold spray deposited Cu (HT-CS-Cu). SKB-Cu was supplied by the Swedish Nuclear Fuel and Waste Management Company (SKB, Solna, Sweden).[35] Both ED-Cu and CS-Cu materials were manufactured in the form of plates. Specifically, a 3 to 4 mm thick Cu coating was deposited onto a 150 mm × 150 mm × 38 mm ASME SA-516 Gr. 70 steel block substrate, Fig. 1. The ED-Cu and CS-Cu were supplied by Integran Technologies Inc. (Mississauga, Canada) and the National Research Council of Canada (Boucherville, Canada), respectively. Figure 1 shows the top and cross-sectional views of an ED-Cu plate.

The specifications of the electrodeposition process have been described elsewhere,[36] and were designed to produce an ultra-fine grain microstructure in the absence of heat-treatment.[34] The cold
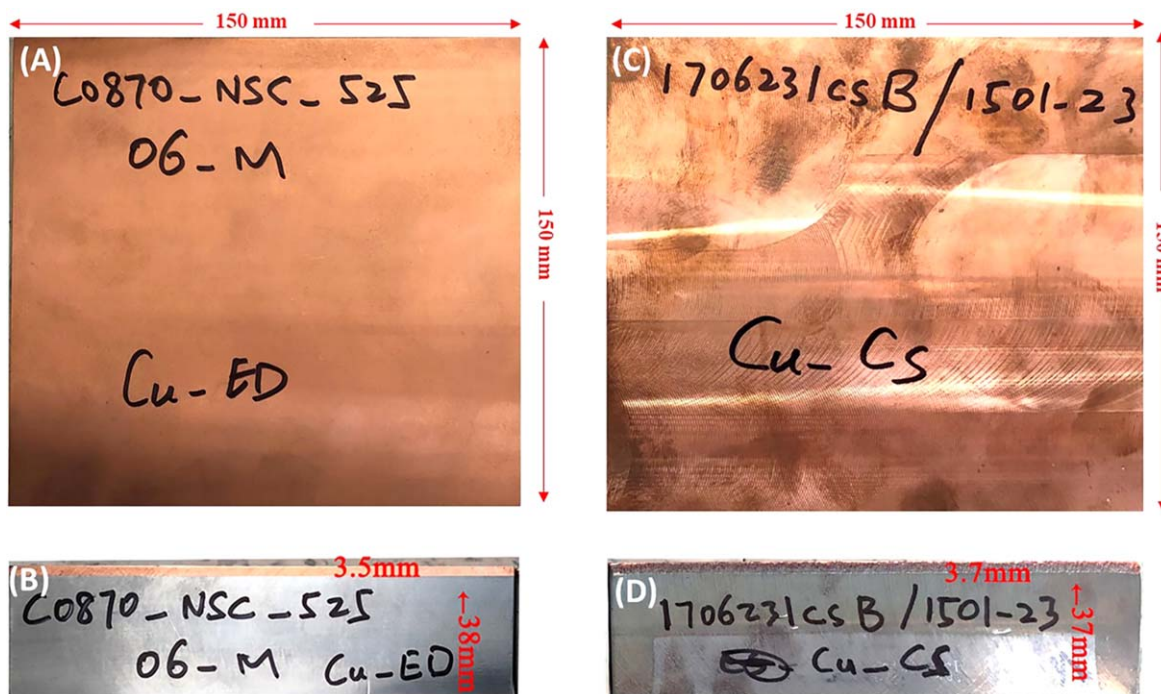
Figure 1. Top surfaces (A) and (C) and cross-section views (B) and (D) of an ED-Cu and AS-CS-Cu plate, respectively, featuring an approximately 4 mm integrally bonded copper coating deposited on a ASME SA-516 Gr. 70 steel plate.

spray process was performed at a gas temperature of approximately 800 °C, with helium (He) gas used for the first coating pass (creating a coating that is approximately 100 μm thick) and nitrogen (N_2) gas for the remainder of the coating.[6,7,13,37] Some of the examined CS-Cu materials were stress-relieved by heat-treating at 350 °C for 1 h after coating deposition to restore ductility.[11]

Specimen and electrolyte preparation.—Cu electrodes were machined as disks from the top surface of each block. A threaded hole was drilled in the back of each disk to allow electrical connection via a stainless steel rod to external circuitry. The drilled hole did not penetrate the Cu surface. The electrode was then set into a Teflon holder using a transparent epoxy resin (Epofix, Struers), leaving only a flat circular surface area of 0.785 cm^2 exposed to the electrolyte during corrosion experiments. The circular surface of the Cu electrode was positioned horizontally with the freshly-polished surface facing down and fully immersed in the electrolyte. Prior to each experiment, the Cu electrode was ground with a sequence of SiC papers with grit sizes of 600, 800, 1000, 1200, 2400, and 4000, and then polished using 3 and 1 μm diamond suspensions in a glycol-based lubricant. The polished surface was rinsed with Type I water with a resistivity of 18.2 MΩ.cm (provided by a Direct-Q® 3UV ultrapure water system, Millipore Sigma), sonicated with methanol (reagent-grade) for 1 min, and dried in a stream of ultrapure (99.999%) N_2 gas.

Prior to microstructural examinations, Cu surfaces were electro-polished using a Struers LectroPol electro-polisher in a solution composed of HNO_3:CH_3OH = 1:3 (HNO_3, ACS reagent, 68%–70%; CH_3OH, ACS reagent) by volume at a temperature of -20 °C. A voltage of 7 V was applied to the specimen for 70 s. Solutions were prepared with reagent-grade sodium chloride (NaCl, 99.0% assay), sodium sulfide ($Na_2S \cdot 9H_2O$, 98.0% assay) and Type I water. Cu electrodes were exposed to solutions containing 0.1 M NaCl + 1 × 10^{-3} M Na_2S with an initial solution pH of 10, a solution selected to facilitate investigation of the short-term (in the range of 5 min to $\sim$ 4 h) sulfide-induced corrosion process. This particular sulfide concentration was chosen to accelerate Cu corrosion, acknowledging that this environment approaches the upper limit of sulfur concentration anticipated in a Swedish DGR,[4,38,39] but significantly exceeds the expected maximum [SH^-] in a Canadian DGR. To ensure a de-aerated environment, solutions were sparged with ultrapure (99.999%) Ar for 30 min prior to each experiment to prevent immediate SH^- oxidation and then continually sparged throughout experiments.

Electrochemical cell and instrumentation.—All electrochemical data were collected using a three-compartment electrochemical cell with an exposed Cu working electrode surface area of 0.785 cm^2 and a total solution volume of approximately 700 mL. A Pt plate connected to external circuitry by a Pt wire (0.5 mm diameter) acted as the counter electrode (CE), and a commercial saturated calomel electrode (SCE, + 0.242 V vs SHE) was used as the reference electrode (RE). When we were conducting experiments, the cell was placed inside a grounded Faraday cage to minimize external electrical interference.

Corrosion and electrochemical measurements.—Corrosion experiments, including corrosion potential (E_{CORR}), linear polarization resistance (LPR), and electrochemical polarization measurements were recorded using a Gamry Interface 1010 E potentiostat (Gamry Instruments Inc., USA) equipped with Echem Analyst (version 7.8.2). Before each experiment was conducted, the Cu electrode was cathodically cleaned at E = -1.5 V vs SCE for 1 min to reduce any air-formed oxides, and then potentiostatically polarized at E = -1.15 V vs SCE for another 1 min to allow the detachment of any H_2 bubbles which may have been formed due to H_2O reduction at the more negative potential. During corrosion experiments, E_{CORR} was recorded as a function of immersion time for a total duration of 24 h, with LPR measurements made every hour, in Ar-sparged

solutions containing 0.1 M NaCl + 1 × 10^{-3} M Na_2S. LPR measurements involved polarizing the Cu electrode ± 5 mV (vs E_{CORR}), at a scan rate of 10 mV/min. The polarization resistance (R_p) values were then calculated from the slopes of the linear current density (i) vs potential (E) plots (i.e., $R_p = \Delta E/\Delta i$).

Most potentiostatic polarizations were conducted at an applied potential of -0.9 V vs SCE for a duration of 5 min to 4 h. This particular potential (-0.9 V vs SCE) was chosen based on its close proximity to the E_{CORR} measured previously in a similar solution, with the intention of introducing only a small perturbation (driving force for corrosion) to the Cu surfaces, thereby facilitating investigation of early-stage sulfide film formation. Cyclic voltammetry (CV) was performed from an initial potential of E = -1.4 V vs SCE to various final potentials at a scan rate of 2 mV/s. Some electrochemical polarizations were reversed at a final potential of -0.4 V vs SCE. All experiments were performed at room temperature (21 ± 2 °C). To ensure reproducibility, all experiments were repeated.

Material characterization.—Before the specimens were exposed to the environment in corrosion tests, SEM coupled with electron backscatter diffraction (EBSD) was conducted to obtain crystallographic texture information of the specimen surface. SEM micrographs and EBSD maps were collected using a FEI NanoSEM 450 at the Reactor Material Testing Laboratory (RMTL) at Queen's University using a Brucker e-flash EBSD detector in combination with the Bruker Quantax Esprit software (version 2.3). During an EBSD analysis, a pre-tilted specimen mounting stage (PELCO 70° pre-tilt holder) was used relative to the normal incidence of the electron beam, thereby enhancing the contrast in the diffraction pattern and the fraction of electrons scattered from the specimen. The accelerating voltage of the electron beam was maintained at 15 or 30 kV while the working distance from the tilted specimen surface to the SEM pole piece was fixed at approximately 15 mm during EBSD acquisition. A minimum misorientation of 2° was used to define a grain boundary. Grain orientations are shown as inverse pole figure (IPF) maps. Step sizes of 1.50 μm, 0.48 μm, and 0.15 μm were used for the as-sprayed cold spray (AS-CS-Cu), heat-treated cold spray (HT-CS-Cu) and electrodeposited (ED-Cu) specimens, respectively. Post-analyses of EBSD maps were conducted using MTEX-5.6.0 toolbox and MATLAB R2020b. In a polycrystalline material, grain boundaries (GBs) are arbitrarily divided into two categories, i.e., a low-angle grain boundary and a high-angle grain boundary.[40,41] Specifically, a low-angle grain boundary (LAGB) is defined by a misorientation angle between two neighbouring grains of ⩽15°.[42] However, if the adjacent grains are misoriented by an angle that is >15°, then the GB is regarded as a high-angle grain boundary (HAGB),[43] resulting in a higher degree of atomic mismatch. The LAGBs and HAGBs are indicated by different colours (LAGBs: dark blue to blue; HAGBs: green to yellow) in grain boundary misorientation maps. Non-indexed areas are shown in black on an IPF map.

Surface micrographs and elemental distributions were obtained on anodically-oxidized Cu specimens using a FEI NanoSEM 450 coupled with a Bruker XFlash EDX detector. Scanning transmission electron microscopy high angle annular dark-field (STEM-HAADF) imaging and STEM-EDX were carried out on selected Cu specimens, which were potentiostatically polarized at a potential of -0.4 V vs SCE for 3.5 h, using a FEI Tecnai Osiris/TEM (STEM) also at (RMTL). EDX data analysis was performed using Bruker Esprit software (version 1.9). The microscope is equipped with 4 Super-X SDD EDX detectors, allowing fast and precise acquisition of X-ray spectra with an excellent signal-to-noise ratio which allows for accurate detection of very small concentrations of elements (<1 at%). Prior to TEM characterization, specimens were prepared using a common lift out procedure on corroded Cu specimens at the Canadian Centre for Electron Microscopy (CCEM) at McMaster University. Specifically, A Zeiss NVision 40 Gemini FIB-SEM (Carl Zeiss, Germany) equipped with a dual-beam Ga$^+$ Focused Ion Beam (FIB) was used to extract TEM foils (80 to 100 nm thick) at specific

film/Cu metal interfaces. STEM-EDX was performed at an accelerating voltage of 200 kV.

Results and Discussion

Characterization of Cu coatings.—SEM micrographs were obtained on electropolished Cu surfaces. For AS-CS-Cu specimens, pores measuring approximately 5–10 μm were visible along interfacial boundaries, Fig. 2A. The distribution of pores and interface boundaries in CS Cu coatings has been observed previously by Tam et al.[44] and Li et al.,[34] demonstrating a heterogeneous microstructure, a high density of dislocations near splat interfaces/boundaries, and pores/cavities throughout the CS-Cu microstructure.[45] Additionally, elongated pores extending the length of several adjacent particles were observed at the junction of a few splat boundaries, Fig. 2A, suggesting that these particle-particle boundaries are weakly bonded. Previously, it has been shown[33] that the presence of splat boundaries (also called inter-particle interfaces or splat-splat interfaces) is due to the deformation of Cu particles, on impingement at a high kinetic energy. As speculated previously,[33,34,46] the corrosion of CS-Cu could propagate differently in the proximity of splat boundaries and/or at open pore areas than on the surface of the bulk material.

Figure 2C shows a SEM backscattered electron (BSE) micrograph of an HT-CS-Cu specimen. As shown by others previously,[13,46] prior to annealing, the CS-Cu coatings exhibited a refined grain size (<3 μm), with splat boundaries visible on the examined surfaces. While the particle interfaces were still visible after annealing, Fig. 2C, they became discontinuous, with discrete scattered circular-shaped pores distributed along the interparticle boundaries. This could be due to the incomplete sintering of the inter-splat areas during cold spray and annealing.[33,46] Notably, small grains (from a few micrometres up to 20 μm) were observed in the interiors of splat boundaries, Fig. 2C, suggesting that microstructural recrystallization occurred during low temperature

annealing (350 °C for 1 h).[33,37] Of the materials characterized by SEM, ED-Cu exhibits a well-refined microstructure, Fig. 2B, with an average grain size of ⩽5 μm; consistent with the observations of Li et al.[34] and Dobkowska et al.[46] No grain boundary defects specific to CS-Cu specimens or pores were observed on ED-Cu, Fig. 2B, suggesting that ED-Cu has lower residual stress than CS-Cu.[47] Figure 2D shows the surface of a SKB wrought Cu specimen, exhibiting large grains (⩾100 μm), as reported by others.[48,49] Although there were no visible pores and particle interfaces on the SKB Cu surface, it should be noted that certain small surface artefacts may have been produced on the SKB Cu during electropolishing.

To examine the microstructure of Cu specimens, EBSD analyses were performed on all three Cu-coated materials. It should be noted that observations and comparisons reported here should be considered qualitative. All Cu specimens exhibited randomly oriented grains, Figs. 3A, 3C and 3E. Of the materials examined, the AS-CS-Cu revealed an unusual heterogeneous microstructure consisting of many ultra-fine small grains distributed along the perimeters of much larger highly deformed grains, Fig. 3A. The highly deformed large grains exhibited gradual variations in colour, indicating a high degree of misorientation throughout the grain. This is likely caused by the high strain rate (up to $10^9 \, \text{s}^{-1}$) inherent to the cold spray process.[34,50] As shown in Fig. 3A, the grain size of AS-CS-Cu varies from a few micrometres up to approximately 50 μm. It is possible that dynamic recrystallization[34] occurred at the particle boundaries, leading to the formation of ultra-fine grains and high-angle grain boundaries (HAGBs).[33,45] This is supported by the observation of high degrees of boundary misorientation angle (⩾40°) around the areas where particle-particle boundaries exist, Fig. 3B. Commonly, the energy of a GB increases as the boundary misorientation angle increases.[42,51] However, the HAGB energy does not behave monotonically with increasing misorientation angle. For instance, there are coincidence site lattice (CSL) boundaries (Σ 3, Σ 5, Σ 7, etc.)
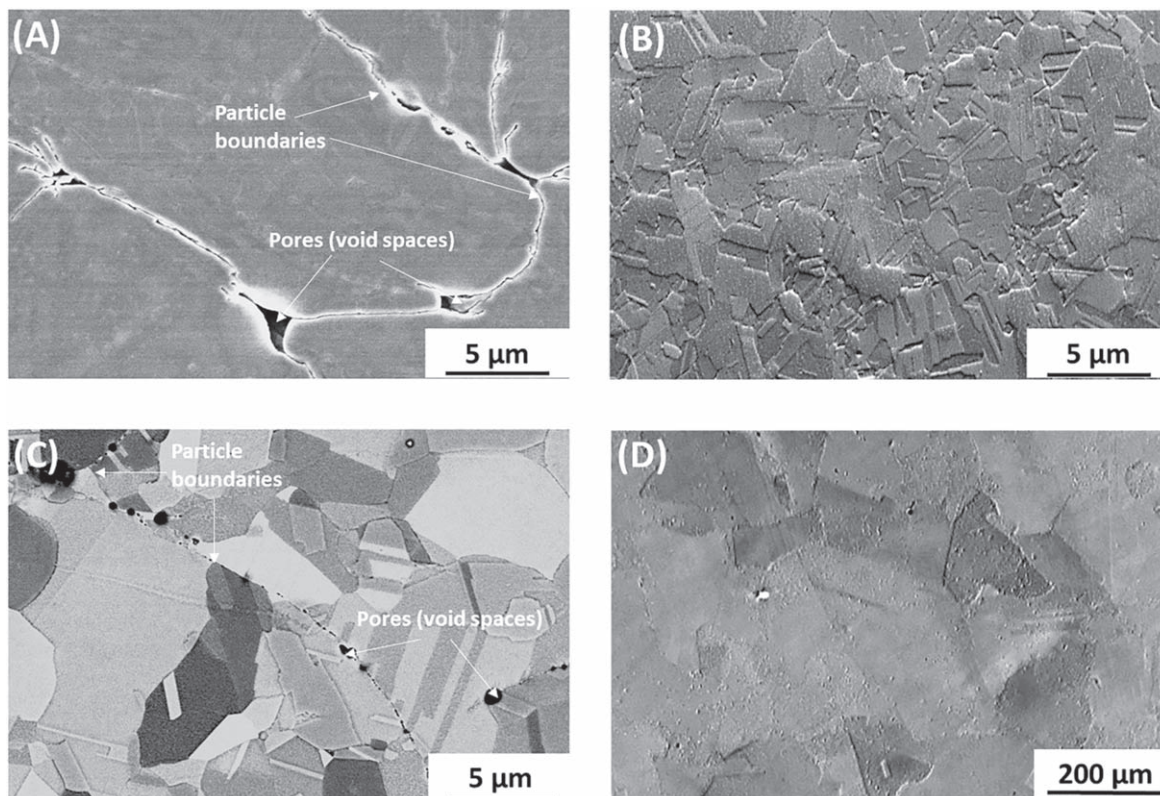
Figure 2. SEM micrographs obtained on electropolished Cu specimens before EBSD analyses: (A) SE image of an as sprayed CS-Cu showing locations of pores and interparticle boundaries, (B) SE image of an ED-Cu showing small grains, (C) BSE image of a heat treated CS-Cu highlighting grains, pores, and particle boundaries, (D) SE image of a SKB-Cu showing large grains (>100 μm).
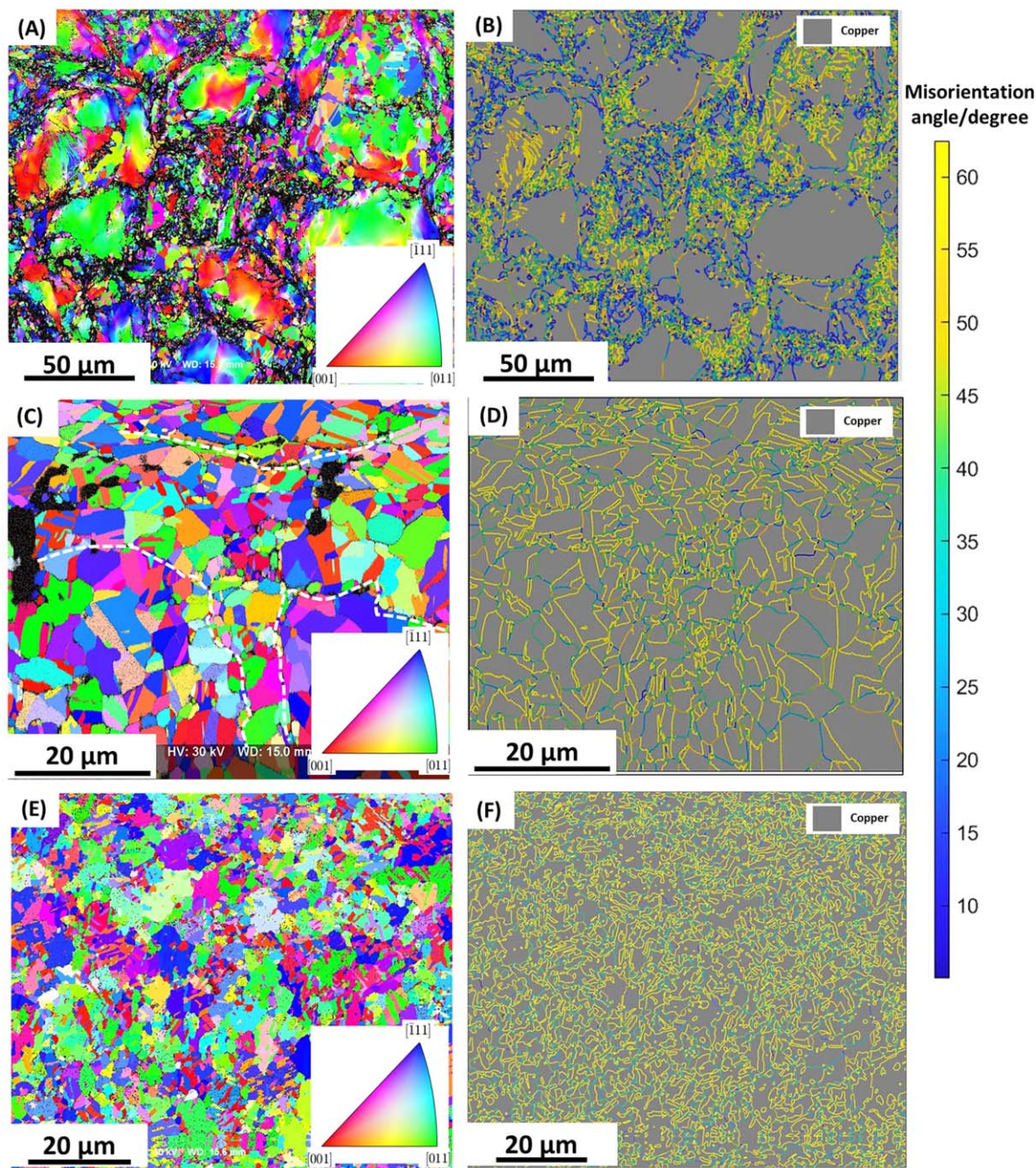
Figure 3. EBSD maps recorded on various Cu coating specimens, including an as sprayed CS-Cu ((A) and (B)), a heat treated CS-Cu ((C) and (D)), and an ED-Cu ((E) and (F)). (A), (C) and (E) are IPF maps showing grain orientations. (B), (D), and (F) are grain boundary misorientation maps of the same areas extracted from EBSD data, with the coloured scale bar on the right showing the misorientation angles in degrees. Note that some particle boundaries are indicated by the dashed curve lines in Fig. 3C.

which exhibit a lower energy despite having a high misorientation angle.[52] A CSL is defined as occurring when lattice sites coincide between the two lattices, with the boundary containing a high density of atomic points with a good atomic fit.[53] Although not shown here, a significant number of Σ 3 coincident site lattice boundaries (CSLs) were formed near the particle boundaries. Since the Σ 3 CSLs generally possess a low boundary energy and a low reactivity,[43,52] the intergranular corrosion resistance of CS-Cu may be improved at certain areas near the particle boundaries.

Figures 3C and 3D shows the grain orientation and boundary misorientation maps of a HT-CS-Cu specimen. Grain growth, possibly due to recrystallization,[34] is visible after annealing for 1 h at 350 °C. In general, the HT-CS-Cu exhibited random texture, with

more well-defined grain features, and showed evidence of grain twinning. It is possible that the large internal strain energy, as previously seen from AS-CS-Cu (Fig. 3A), resulted in recrystallization and subsequently the formation of smaller grains.[44] In addition, areas situated near the particle boundaries, as indicated by the dashed curves (Fig. 3C), did not exhibit the ultra-fine grain features seen on AS-CS-Cu. This is consistent with the observations made by Li et al.,[34] indicating that no nano size grains were present near the particle boundaries after heat treatment. As observed for AS-CS-Cu, Fig. 2A, distinct particle boundaries remained visible in HT-CS-Cu, Figs. 2C and 3C, although they appeared more discontinuous and dispersed across the surface. The non-indexed areas (shown in black), Fig. 3C, could be attributed to the presence of open pores on

the surface. When we inspected the grain boundary misorientation map, Fig. 3D, it was clear that the vast majority of the HT-CS-Cu surface exhibited a significant proportion of HAGBs. Although not shown here, Σ 3 coincident site lattice boundaries (CSLs) coincided with most of the HAGBs of the HT-CS-Cu. These results indicate that the overall corrosion resistance of HT-CS-Cu could be improved in spite of the presence of a significant number of HAGBs (i.e., CSLs are low-energy interfacial regions).

The most refined microstructure, with a reported average grain size ranging from 1.2 to 3.3 μm,[33,34,46] was observed in ED-Cu, Fig. 3E. Many smaller grains existed within randomly oriented large grains. As shown in the IPF map, Fig. 3E, the vast majority of the grains were oriented towards {111} and {011}. In addition, the grains oriented to {001} were smaller and randomly distributed throughout the analyzed area of the ED-Cu. Unlike the CS-Cu specimens (Figs. 3B and 3D), ED-Cu exhibited a denser distribution of HAGBs across the surface and significantly fewer LAGBs, Fig. 3F, with the majority of the GBs corresponding to the Σ 3 CSLs.

Corrosion measurements of Cu coatings.—Figure 4 shows E_{CORR} values measured on the AS-CS-Cu, HT-CS-Cu, ED-Cu and SKB-Cu specimens in Ar-sparged solutions containing 0.1 M NaCl + 1 × 10^{-3} M Na$_2$S. As noted above, the selected sulfide concentration was significantly higher than that anticipated in an actual DGR,[1,2,16,54] to accelerate corrosion and determine whether microstructural heterogeneities were relevant. The E_{CORR} of SKB-Cu was the lowest and increased rapidly during the first hour, to a steady-state E_{CORR} value at ~-0.95 V vs SCE after 4 h. The E_{CORR} values of ED-Cu and HT-CS-Cu exhibited very similar trends, with a rapid initial increase followed by a slower longer-term slight decrease. In particular, the E_{CORR} of ED-Cu decreased slightly more rapidly than that of HT-CS-Cu, with a minimum value slightly lower (-0.94 V vs SCE) than that recorded for the HT-CS-Cu (-0.93 V vs SCE). These close similarities suggest that the general corrosion behaviour of these materials is very similar. By comparison, the AS-CS-Cu exhibited a different behaviour, with E_{CORR} initially rising rapidly to approximately -0.85 V vs SCE before decreasing slowly to -0.90 V vs SCE, with fluctuations in values observed throughout the experiment. These fluctuations in E_{CORR} may be due to the heterogeneity of the AS-CS-Cu surface, as shown in Figs. 2 and 3, on which high energy sites (i.e., interfacial regions or pores) yield slight variations in the corrosion rate. Also shown in Fig. 4, is the equilibrium potential ($E^e = -1.01$ V vs SCE) for Cu/Cu$_2$S for this particular [SH$^-$] (1 × 10^{-3} M Na$_2$S).[55] Overall, E_{CORR} values were close to E^e, as observed previously by Chen et al.[21] and Guo et al.,[56] indicating the formation of chalcocite (Cu$_2$S), as demonstrated previously using X-ray diffraction (XRD).

Table I shows the average R_p values measured over a 24 h exposure period once E_{CORR} approached its steady-state value. The apparent corrosion rate ($\propto R_p^{-1}$) was lowest on ED-Cu and SKB-Cu specimens and considerably higher on the AS-CS-Cu, with an intermediate value for the HT-CS-Cu. Based on Fig. 4 and Table I, no apparent relationship between E_{CORR} and R_p was observed. This indicates that the differences in R_p cannot be explained by a simple rebalancing of the relative rates of the anodic and cathodic half reactions. These changes in R_p between the different Cu materials suggest a clear influence of surface properties on the corrosion rate, with the highly defective AS-CS-Cu exhibiting the highest rate. The lower rate for HT-CS-Cu, and its approach to the values recorded on the ED-Cu and SKB-Cu, indicate a clear improvement when the macroscale defects on the cold sprayed Cu surface were removed by annealing.

Electrochemical measurements of Cu coatings.—To investigate the electrochemical behaviour of CS-Cu coatings, two sets of CVs were performed, to different upper potential limits, on stationary HT-CS-Cu and AS-CS-Cu electrodes in Ar-sparged solutions containing 0.1 M NaCl + 1 × 10^{-3} M Na$_2$S, Fig. 5. When the potential on the HT-CS-Cu was scanned to a maximum of -0.85 V vs SCE
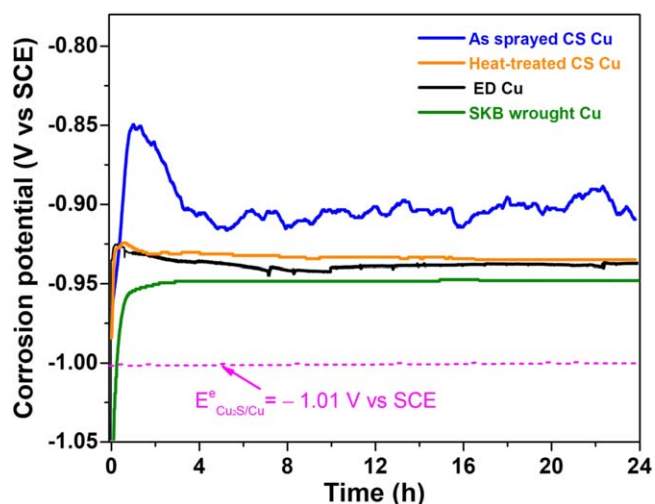
Figure 4. Corrosion potential (E_{CORR}) measurements recorded on various types of Cu materials as a function of time in Ar-sparged solutions containing 0.1 M NaCl + 1 × 10^{-3} M Na$_2$S.

(i.e., to approximately 120 mV more positive than the E_{CORR}) the current rose to a plateau value (A1) and did not decrease at higher potentials as would have been expected if passivation occurred, although the lower current in this region on the negative-going scan showed that the film formed was partially protective, previous work has demonstrated the porous nature of this film.[18,19,27,57] The anodic current (A1) and the corresponding cathodic peak (C1) can be attributed to the formation and subsequent reduction of a Cu$_2$S (chalcocite) film, as demonstrated previously.[18,58] Previous studies have shown that film formation was diffusion-controlled.[57] To maintain a diffusion-controlled growth process, the sulfide film must be porous, allowing a rapid transport of Cu(I) (as soluble sulphide complexes and clusters) from the metal surface to the film/solution interface, leading to further film growth. To maintain growth at the film/solution interface, transport within the pores in the film must not be blocked by their closure, which would lead to control of film growth by cation transport through microscopic defects in the film.

On the negative-going scan, Fig. 5A, a single, almost symmetrical cathodic peak for the reduction of Cu$_2$S was observed at -1.08 V vs SCE on HT-CS-Cu. Although not shown here, features associated with the C1 peak were similar to those observed on SKB-Cu in the identical solution environment.[19] The amount of Cu$_2$S formed, expressed as a charge (Q), was obtained by calculating the area associated with the anodic current region A1. Similarly, the amount of anodically-formed Cu$_2$S that was reduced, was represented by the charged integrated under the area of the reduction peak C1. As observed previously,[18] the amount of charge associated with film formation (A1) was approximately equivalent to the charge recovered by film reduction (C1), demonstrating that all of the anodically-formed Cu$_2$S on the positive-going scan was effectively reduced on the reverse scan.

The AS-CS-Cu exhibited similar behaviour (A1′) but anodic oxidation commenced at a lower potential than on the HT-CS-Cu, with the current maintained in region A2′ at more positive potentials, Fig. 5A. This early onset of anodic oxidation could suggest that the AS-CS-Cu is more susceptible to corrosion, due to the defective surface. On the negative-going scan, only a single cathodic reduction peak was observed at -1.1 V vs SCE, due to the reduction of the anodically-formed Cu$_2$S. As observed with HT-CS-Cu, the charge associated with anodic film formation (A1′ and A2′) was approximately equal to the charge associated with film reduction (C1′), again confirming that all the anodic charge went to Cu$_2$S film formation.

When the scan was extended to -0.4 V vs SCE, Fig. 5B, the current was maintained throughout region A2 (A2′) leading to more

Table I. Average R_p values measured after E_CORR approached its steady-state values in Ar-sparged solutions containing 0.1 M NaCl + 1 × 10⁻³ M Na₂S.

Material	R_p ($\Omega \cdot cm^2$)
As sprayed CS Cu[a)]	1934 ± 100
Heat-treated CS Cu	3032 ± 55
ED Cu	6900 ± 63
SKB wrought Cu	6523 ± 40

a) due to the fluctuation of the corrosion potential measured on as-sprayed CS Cu, the extrapolated R_p value may only be approximate.
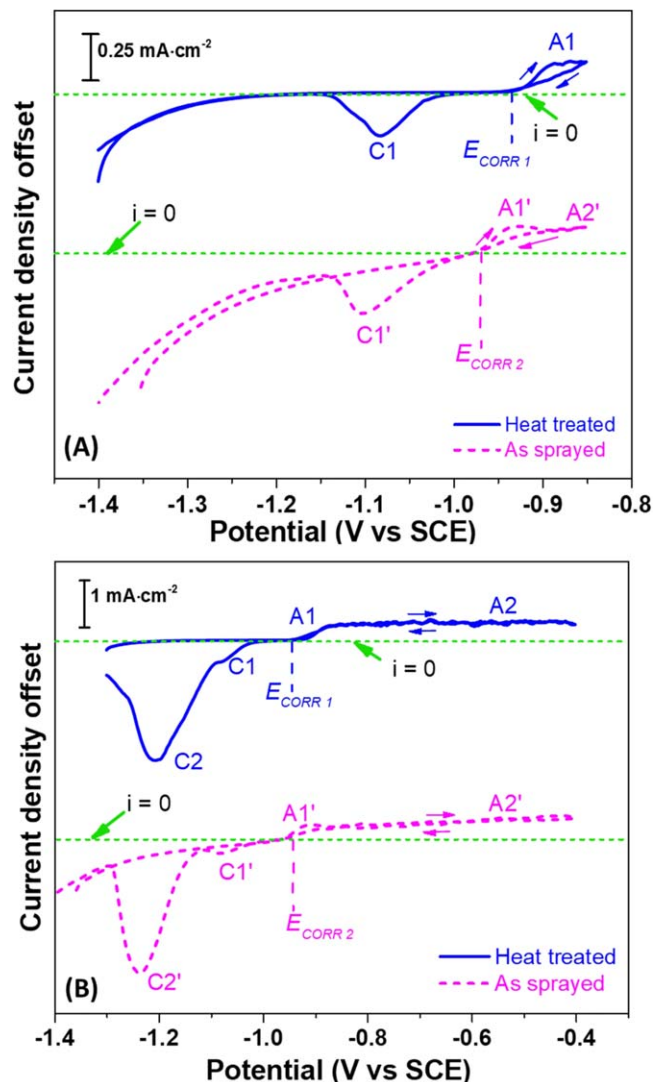
Figure 5. CVs recorded on heat treated and as sprayed CS Cu samples to two different upper potential limits in solutions containing 0.1 M NaCl + 1 × 10⁻³ M Na₂S: (A) CVs scanned to the maximum potential of −0.85 V vs SCE, (B) CVs scanned to the maximum potential of −0.4 V vs SCE. The E_CORR and various anodic and cathodic peaks are labeled with A1, A2, A1′, A2′, C1 and C2. Blue and pink arrows indicate the scanning direction of each CV. Note that both figures were plotted using linear Y-axis.

extensive film reduction on the reverse scan (C1/C2 and C1′/C2′). As seen previously, extending the scan to this potential leads to further Cu₂S formation,[19,59] with the formation of oxides, hydroxides and soluble chloride complexes thermodynamically prohibited in this potential range.[29,60,61] As shown in Fig. 5B, on the negative-going scan, the anodic current retraced its original path through

regions A1/A1′ and A2/A2′, confirming that Cu₂S film growth continued, and demonstrating that the sulfide film formed on the forward scan did not passivate the Cu surface. Such a feature would only have been possible if the Cu₂S film remained porous and able to sustain film growth at the Cu₂S/solution interface, a process supported by the transport of Cu(I) species through solution, as sulfide complexes (Cu(SH)₂⁻) and Cu₃S₃ clusters.[17,62] In addition, film reduction occurred in two stages, with a small cathodic reduction peak C1/C1′ and a much larger reduction peak C2/C2′ being observed on both CS-Cu specimens, Fig. 5B. This suggests the presence of two distinct morphological forms of the same phase since previous XRD results demonstrated that only chalcocite (Cu₂S) was formed.[18,21,56] This dual layer film formation process has been studied in detail previously.[19] This study showed that peak C2/C2′ could be attributed to the reduction of crystalline Cu₂S deposited on top of the initially formed Cu₂S layer reduced at peak C1/C1′. Overall, both types of CS-Cu exhibited similar electro-chemical behaviour, which did not distinguish between possible differences in corrosion behaviour that may occur at high energy defect sites, such as splat boundaries or pores.

Short-term (up to 800 s) potentiostatic polarizations were performed at −0.9 V vs SCE on the various Cu specimens, Fig. 6. This polarization potential was chosen based on the E_CORR measurements in Fig. 4, so that the electrochemical driving force,[63] was as close as possible to the natural corrosion condition recorded on the various Cu materials. As shown in Fig. 6, the current was initially high (0.1 to 0.2 mA cm⁻²) for SKB-Cu, HT-CS-Cu and ED-Cu, and decreased rapidly during the first 50 s to a steady-state value of approximately 70 μA cm⁻². At very short times this can be attributed to the non-Faradaic process of double layer charging but beyond approximately 1 s to a combination of the onset of partial control by SH⁻ transport to the Cu surface and the formation of a partially inhibiting Cu₂S film which subsequently thickened under partial transport control. The initial current values (t ⩽ 30 s) ranged from 50 to 200 μA cm⁻² and may reflect the differences in reactivity of the SKB-Cu, HT-CS-Cu and ED-Cu surfaces, with the CS-Cu being initially most reactive and ED-Cu the least. Beyond ∼ 450 s, the steady-state currents became effectively indistinguishable (∼ 80 μA cm⁻²). These steady-state current values indicate that the growth of a non-passivating film under partially transport-controlled conditions was similar on the three Cu materials. For a truly passive film, a current of approximately 1 μA cm⁻² would be expected.[64] Additionally, the observation of minor fluctuations in current throughout the experiments suggests the films formed were slightly unstable.

The current transient recorded on AS-CS-Cu exhibited significantly different behaviour, the initial current being approximately one order of magnitude smaller than on the other materials. Over approximately 75 s the current rose to a value close to that of the other materials before slowly decreasing to a value of approximately 30 ± 5 μA cm⁻². Noticeably, significant fluctuations in current over the range approximately 10 and 60 μA cm⁻² persisted throughout the measurement, suggesting that the heterogeneous microstructure, specifically the presence of high energy defect sites (dislocations density and particle-particle boundaries[33,50]) shown in Figs. 2 and 3, has a significant influence on the material reactivity.

Table II shows the average sulfide film thickness values calculated based on the total charge obtained by integrating the current-time profiles from Fig. 6, and the assumption that the films are of uniform thickness. The detailed conversion from charge to the average film thickness is described elsewhere.[65] The estimated film thickness values ranged from 46 nm on AS-CS-Cu to 83 nm on SKB Cu. The values recorded on the HT-CS-Cu, SKB-Cu and ED-Cu were very similar, consistent with the similarities in E_CORR (Fig. 4) and the polarization currents (Fig. 6). The thickness of the film on the AS-CS-Cu was considerably lower, indicating a less reactive surface. This suggests that the heterogeneous nature of AS-CS-Cu with the presence of pores and interfacial splat boundaries, may have caused altered corrosion kinetics near these non-uniform areas leading to a different corrosion rate. In addition, the small thickness
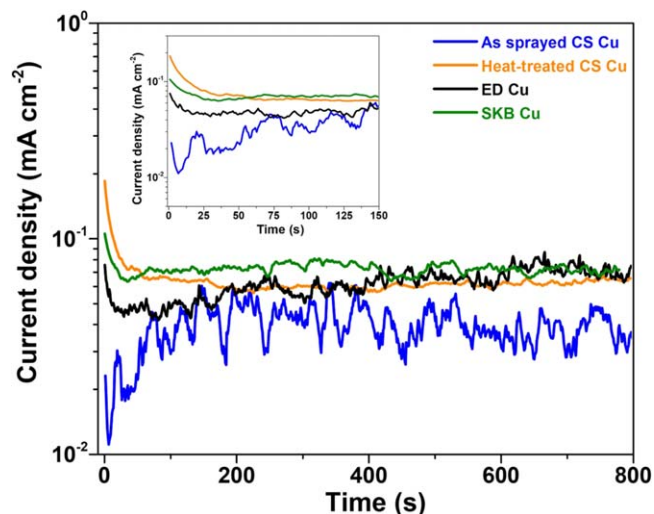
Figure 6. Current evolution as a function of time recorded on various Cu materials during potentiostatic polarization at the potential of −0.9 V vs SCE.

values of AS-CS-Cu may also be due to the smaller perturbation ($E_{applied}$ − E_{CORR}) exerted on the AS-CS-Cu surface compared to that of the other Cu materials.

Characterization of electrochemically polarized Cu surfaces.—
Scanning electron microscopy on anodically oxidized Cu coatings.—
Figure 7 shows SEM micrographs recorded on AS-CS-Cu and ED-Cu specimens for films grown potentiostatically at −0.9 V vs SCE for 800 s in a 0.1 M NaCl + 1 × 10^{-3} M Na$_2$S solution. As shown in Figs. 7A and 7B, a very thin nodular film was formed on AS-CS-Cu. While this film was uniformly distributed across the surface, Fig. 7A, open pores and particle boundaries were clearly visible on the surface. Examination of the areas surrounding and in the open pores on AS-CS-Cu, Fig. 7B, showed that, at micro-scale resolution, no corrosion products were visible inside the open pore, but were deposited on the outer edge of the pore. The absence of any distinguishable corrosion products within the pore suggests that the corrosion front did not propagate into the occluded areas, although nanoscale analyses are required to confirm whether this is the case (Section 3.4.2). Although further confirmation is required these observations suggest that the nodular nature of the deposited film may be related to the heterogeneous microstructure of the surface, shown to be composed of ultra-small grains along the perimeter of much larger deformed grains, Fig. 3A.

To determine the composition of the deposit on the outer surface, an SEM-EDX analysis was performed on the nodular deposit (within the area marked with a red circle in Fig. 7B). To minimize the analytical penetration depth (working volume), the acceleration voltage of the primary electrons was maintained at 10 kV when collecting EDX spectra. The EDX spectrum exhibited a strong signal for S at 2.3 keV and a very weak signal for O at 0.5 keV, confirming the presence of Cu$_2$S and a negligible amount of Cu oxides. The percentages by weight of O and S were 1.2% and 34.8%, respectively, with the former considered close to the background level, given the elemental sensitivity for O. The absence of a signal

for Cl in this spectrum and others recorded on surfaces, indicates minimal, if any, CuCl formation, consistent with thermodynamic expectations in the presence of sulfide at the concentration used.[60]

The ED-Cu specimen exhibited a surface morphology different to that of AS-CS-Cu, Figs. 7C and 7D. The film, while still non-uniformly distributed, comprehensively covered the surface. It should be noted that electropolishing was conducted on Cu surfaces prior to performing any electrochemical experiments. Its effect is presently unclear. Close inspection of the images in Figs. 7C and 7D suggests that growth may have been more extensive along grain boundaries. It is possible that anodic oxidation favoured areas containing HAGBs, consistent with the observation from Fig. 3F, which showed a high density network of such boundaries on the ED-Cu surface. That HAGBs on Cu surfaces are preferential corrosion sites relative to the lower energy grain surfaces has been proposed by Miyamoto et al.[31] and Dobkowska et al.[46] On the time scale of the present experiments, the relative increase in corrosion rate at HAGBs appeared minor. The nodular form of the Cu$_2$S deposit on the AS-CS-Cu suggests that the film is less protective than that formed on the ED-Cu, which is apparently inconsistent with the lower current density measured in growing the AS-CS-Cu film, Fig. 6, and with the R$_P$ values measured on open circuit, Table II. However, E$_{CORR}$ measured on AS-CS-Cu is ∼ 200 mV more positive than that measured on the other Cu specimens., Fig. 4. As a consequence, the overpotential on the AS-CS-Cu at an applied potential of −0.9 V would be considerably lower than on the other three specimens, which would account for the lower current density and lower "apparent" film thickness, Table II, despite the higher corrosion rate (R$_P^{-1}$), Table II. Thus, the higher corrosion rate on the AS-CS-Cu can be attributed to the formation of a much less protective nodular film.

Site-Specific FIB Extraction and Transmission Electron Microscopy on Anodically Oxidized Cu Coatings

To investigate the nanoscale composition and structure of the anodic films grown on Cu, a site-specific lift out technique was applied to prepare TEM specimens using a dual beam Ga$^+$ FIB-SEM on corroded AS-CS-Cu to determine whether open cavities and high energy splat regions were preferential sites for corrosion. Of particular interest are the morphological and elemental distributions across the film/Cu interface at the surface and at splat interfaces. Figure 8 shows the steps involved in the FIB lift out technique used to create a working TEM foil at the film/AS-CS-Cu interface. Prior to foil preparation, the AS-CS-Cu was potentiostatically polarized at −0.4 V vs SCE (region A2′ in Fig. 5) for 3.5 h in an Ar-sparged solution containing 0.1 M NaCl + 1 × 10^{-3} M Na$_2$S. To limit decomposition of sulfide films under both electron and Ga ion beams,[29] the selected area on the surface, Fig. 8A, was first plated with an amorphous carbon (C) layer via electron beam deposition at an accelerating voltage of 3 kV. A tungsten layer (approximately 3 μm) was then deposited on top of the C layer, further preventing film decomposition. FIB milling was then performed to create trenches surrounding the area of interest, Fig. 8B. The prepared specimen was then lifted out from the FIB-milled area using a micromanipulator, Fig. 8C. Immediately following lift out, the specimen was attached to a Cu TEM grid, as shown in Fig. 8D. The final step, Fig. 8E, involved removing excess material at the interface to thin the specimen to the electron transparency

Table II. Average film thickness calculated based on the charge integrated from current-time profiles in Fig. 6.

Material	Charge Density (mC cm^{-2})	Film Thickness (nm)
As sprayed CS Cu	31.1	45.8
Heat-treated CS Cu	52.4	77.2
ED Cu	48.3	71.1
SKB wrought Cu	56.0	82.5
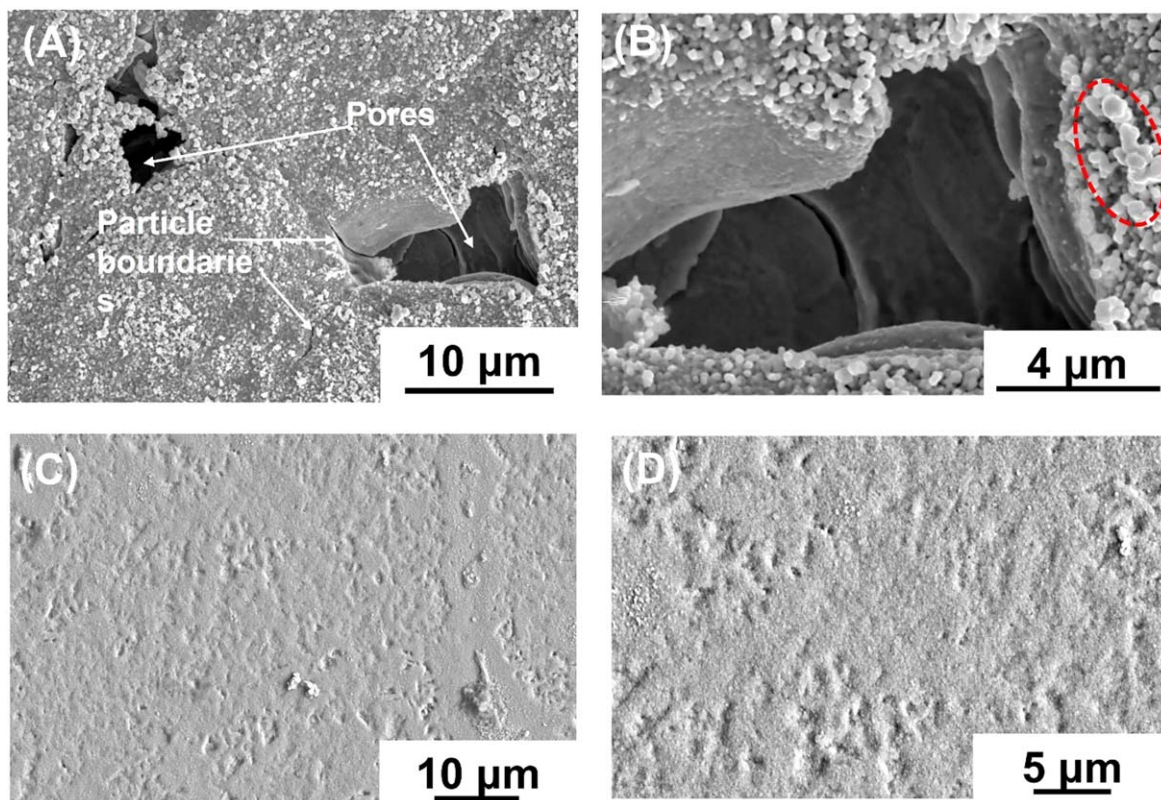
Figure 7. SEM micrographs recorded in SE mode of an as sprayed CS-Cu (A and B) and an ED-Cu (C and D) after potentiostatic polarizations at −0.9 V vs SCE for 800 s in solutions containing 0.1 M NaCl + 1 × 10^{-3} M Na$_2$S. Arrows indicate regions where there are pores and particle boundaries on the as sprayed CS-Cu. The red dashed circle shows the area where EDX analysis was performed.

(<100 nm) required for TEM analysis. Figure 8F is a SEM micrograph taken at the interface shown in Fig. 8E, showing the presence of a thin surface film, as indicated by the orange arrows, and the particle boundaries at the interface, as indicated by the white arrow. This interfacial region was purposely targeted to evaluate whether corrosion occurred at the nanoscale in the localized area where a cavity/splat interface was present.

Figure 9 shows a STEM-HAADF image and the corresponding STEM-EDX maps obtained at the tip area of a particle boundary on the anodically oxidized AS-CS-Cu. This particle boundary was extracted near the cross-section shown in Fig. 8F. The dominant EDX signal for Cu was observed on the surface except for the areas within the particle boundary. O, S, and some C were distributed in the proximity of the tip and other areas away from the particle boundary, with O exhibiting a strong signal, Fig. 9D. Strong signals for C were also seen within the particle boundary, Figs. 9E and 9F. It is unclear why C was enriched (51% by weight) in area 1, Fig. 9F), and was still observable after the Cu surface had been polarized. A possibility was that C was an artefact caused by contamination during C layer deposition at the start of foil preparation or even during transfer of the TEM foil from the FIB-SEM. Equivalent amounts of O and S, accounting for 5.2% by weight, were seen in area 2, Table III, suggesting the presence of both sulfide and oxide films at the particle boundary tip. In addition, although not shown here, a distinct S peak was observed in the EDX spectrum from area 2, confirming small concentrations of S at the tip. Therefore, these results indicate that minor quantities of SH$^-$ do penetrate the porous location at splat interfaces on the surface, even during the early stages of exposure to sulfide solutions, leading to the incomplete conversion (over this exposure time frame) of the oxide on the boundary surfaces to sulphide. The effect of this SH$^-$ ingress on material or mechanical properties is presently unknown. Further work is underway to determine whether SH$^-$ penetration occurs in less aggressive solutions containing sulfide, that better simulate DGR conditions.

STEM-EDX analysis was also performed at the cross-section of the anodically oxidized AS-CS-Cu, Fig. 10. The arrow on top of the STEM-HAADF image in Fig. 10A indicates the position of each phase across the interface. A two-layer film structure was visible, and the corresponding elemental distributions are shown in Fig. 10. S signals were dominant throughout the film, with the inner layer (area 2, Fig. 10F) exhibiting a much more pronounced intensity. In addition, the elemental distributions of S and Cu coincided, confirming the films were composed of mostly copper sulfide. Examination of the O map in Fig. 10D and Table IV, shows that small amounts of O (3.6% by weight), were present in the outer-layer of the film, most likely due to air-oxidation during specimen transportation. Although qualitative elemental analysis was not performed in the local areas situated right beneath area 2 (marked with a red circle in Fig. 10F), a minor O signal was observed. As suggested above for inter-particle boundaries, this may be attributed to the inherent impurities from the manufacturing process associated with the as sprayed CS Cu,[44] as O is one of the major non-metallic impurities present within the CS Cu coatings.

Although experiments were performed in aerated nitric acid solutions, the rankings of corrosion rates of Cu materials observed in our study were in the same order as they were observed by Dobkowska et al.,[46] with the ED-Cu and the AS-CS-Cu demon-strating the highest and lowest corrosion resistance, respectively, indicating that inter-particle boundary faults and porosity on AS-CS-Cu could act as preferential pathways for corrosion propagation.

To summarize, the nanoscale characterization of the local chemistry at the splat/interparticle boundary showed that minor amounts of S were present at the boundary tip on the anodically-oxidized AS-CS-Cu. This provides evidence that the diffusion/ingress of SH$^-$ into pores and fractures had occurred and may
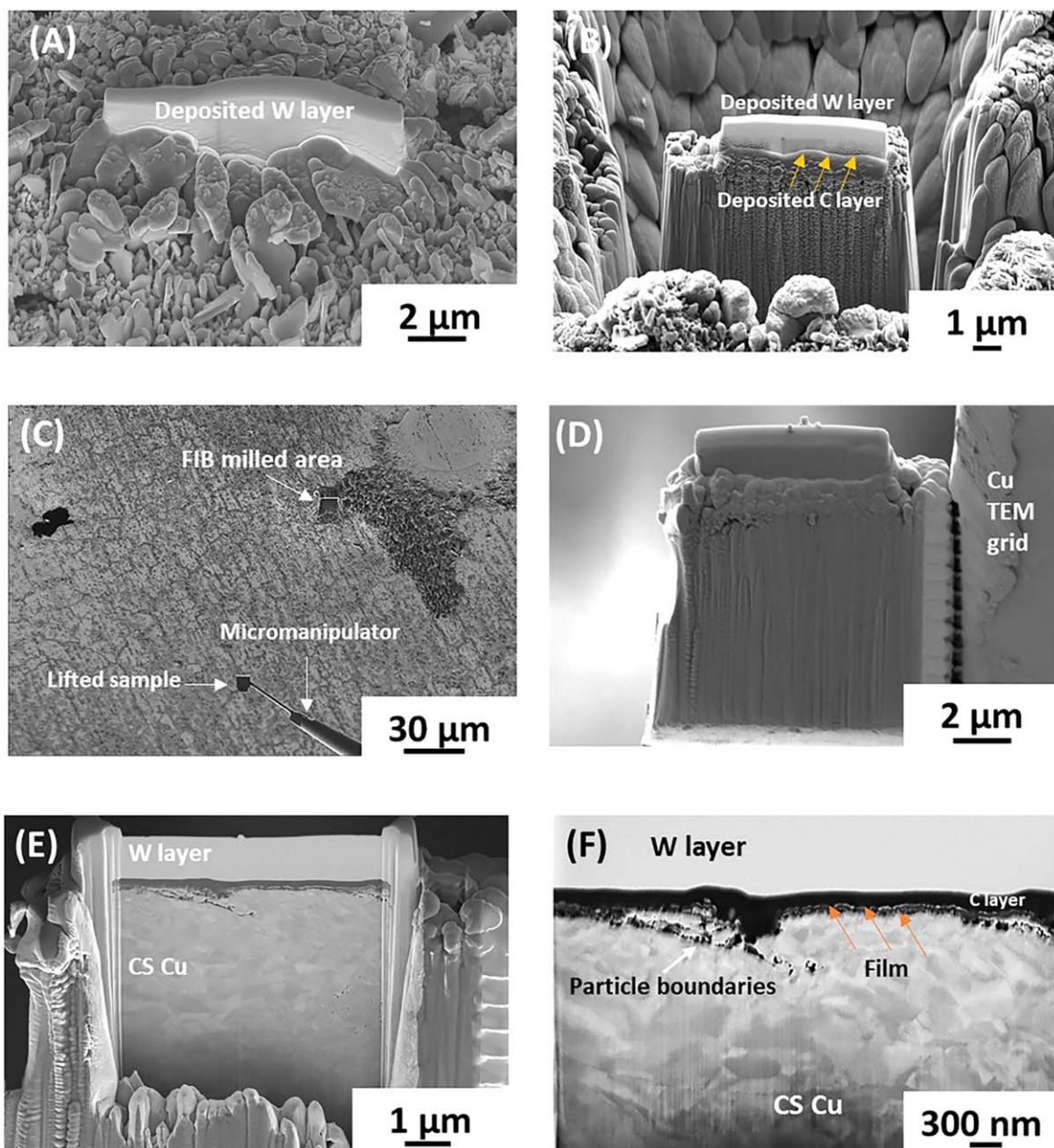
Figure 8. Focused ion beam (FIB) lift out technique, used to create a working TEM foil at the film and as sprayed CS-Cu interface. Photos are labelled chronologically from (A)-(F). (A) Location of a surface film that was preserved by the deposition of both a tungsten (W) and an amorphous carbon (C) layer, with clear observation of W layer only. (B) FIB milling around the area of interest while the surface film was protected by the deposited W and C layer on the top surface. (C) Sample was lifted out using a micromanipulator. (D) Sample was mounted to a Cu TEM grid. (E) Sample was thinned to electron transparency in preparation for TEM analysis. (F) a high resolution image obtained at the FIB-Cut cross-section on the same sample as shown in (E), indicating the presence of a thin surface film and particle boundaries at the interface.

have induced corrosion at splat interfaces or cavities. In these short-term experiments, this appears to have been dominantly the reaction of SH^- at the O-decorated particle interfaces. It should be noted again that the $[SH^-]$ was well above that expected in the Canadian DGR and the penetration depth was shallow (100 s of nm). Nanoscale characterization was required to identify localized ingress, and demonstrates the benefit of characterizing corrosion using complementary techniques that provide insight into the nanoscale chemistry and electrochemistry. Previous application of only microscale analytical techniques (SEM/EDX and XRD) for the elucidation of surface film compositions and materials corrosion performance could not demonstrate the distribution of very small quantities of elements within confined areas; i.e., at splat interfaces. A more comprehensive nanoscale investigation of corrosion in solutions

with the much lower $[SH^-]$ anticipated under Canadian DGR conditions ($\leqslant 10^{-6}$ M) is underway. It is also necessary to study the early stages of the corrosion process under open circuit, as opposed to electrochemically polarized, conditions, since the balance between surface reactivity and transport (of SH^-, $Cu(SH)_2^-$ and Cu_3S_3) will be different.

Conclusions

• The early-stages of corrosion of various Cu materials were examined in solutions containing 0.1 M NaCl + 1×10^{-3} M Na_2S using microscale analytical techniques, i.e., SEM/EBSD in combination with electrochemical techniques, followed by the application
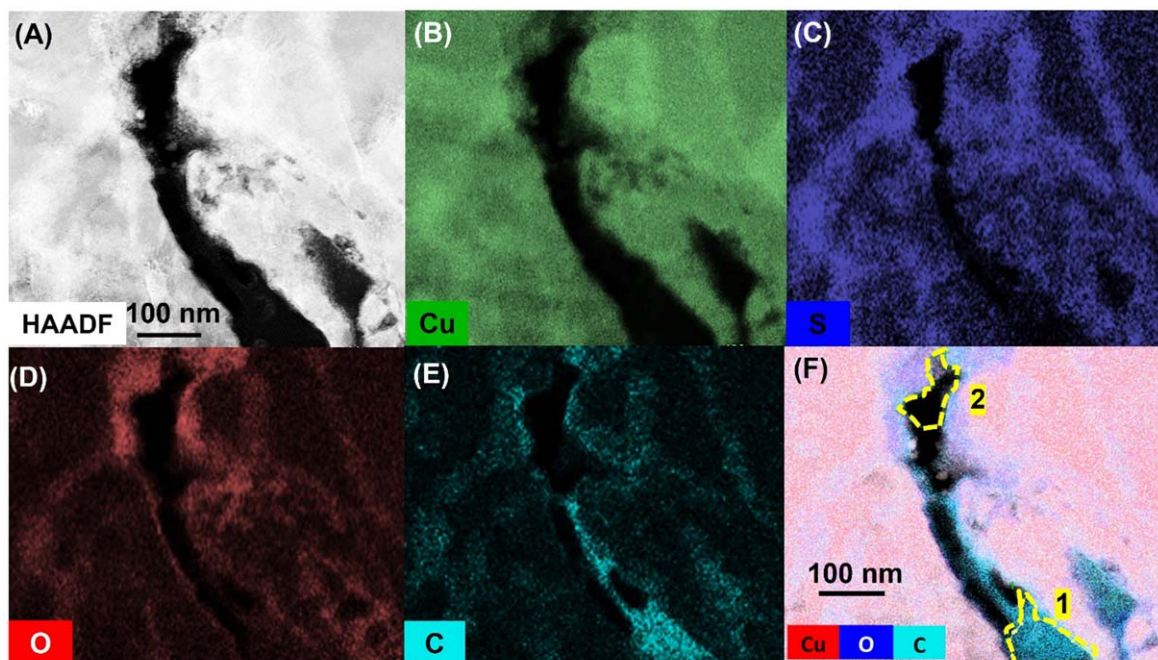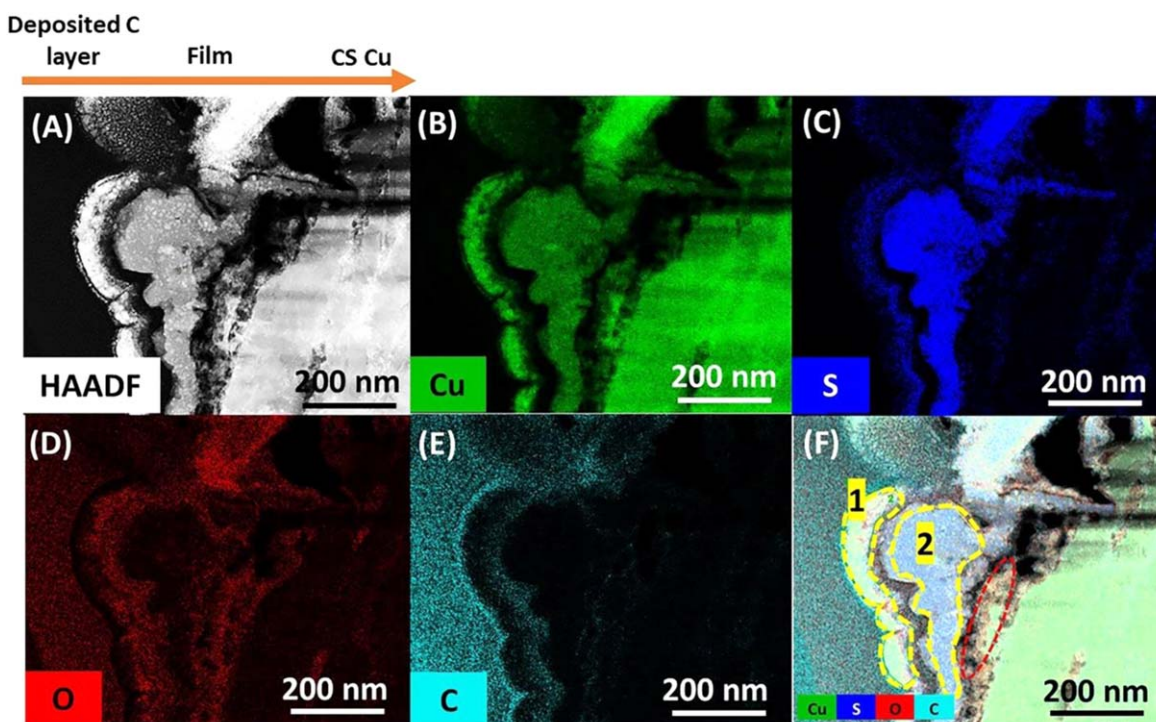
Figure 9. STEM-HAADF image and EDX elemental maps recorded at an interparticle boundary of a corroded as sprayed CS-Cu after potentiostatic polarization at the potential of -0.4 V vs SCE for a total duration of ~ 3.5 h in a solution containing 0.1 M NaCl + 1×10^{-3} M Na$_2$S. This particle boundary was extracted at the cross-section shown in Fig. 8F. Areas 1 and 2 were two localized regions where the wt% of each element was extracted, see Table III. Note that the colour code of each element in Fig. 9F was different from the rest of elemental maps.

of STEM-EDX to investigate the nanoscale chemistry on an anodically oxidized AS-CS-Cu specimen.

• Of the Cu materials examined, AS-CS-Cu exhibited a distinct heterogeneous microstructure, consisting of splat/inter-particle boundaries and open pores. In addition, EBSD analyses revealed a significant amount of grain deformation across the examined

AS-CS-Cu surface. By comparison, HT-CS-Cu exhibited well-defined grain features with a lower density distribution of splat boundaries and pores, and the presence of annealing twins (Σ 3 CSLs). Unlike the CS-Cu specimens, ED-Cu consisted of extremely fine grains and a dense network of HAGBs that coincided with Σ 3 CSLs. Despite having a high misorientation angle at the GB, Σ 3

Figure 10. STEM-HAADF image and EDX elemental maps recorded at a film/CS-Cu interface of a corroded as sprayed CS-Cu after potentiostatic polarization at the potential of -0.4 V vs SCE for a total duration of 3.5 h in a solution containing 0.1 M NaCl + 1×10^{-3} M Na$_2$S. This interface was extracted from the cross-section shown in Fig. 8F. Note that areas 1 and 2 were two localized regions where the wt% of each element was extracted, see Table IV.

Table III. STEM-EDX analysis of two local areas of the particle boundary shown in Fig. **9**F. Concentrations are reported as weight percentages.

Element Location	Cu	S	O	C	Sum
Area 1	38.0	1.6	9.4	51.0	100.0
Area 2	83.4	5.2	5.2	6.2	100.0

Table IV. STEM-EDX analysis of two local areas at the cross-section of an anodically-oxidized AS-CS-Cu shown in Fig. **10**F. Concentrations are reported as weight percentages.

Element Location	Cu	S	O	C	Sum
Area 1	92.2	2.6	3.6	1.6	100.0
Area 2	89.4	9.6	0.8	0.2	100.0

CSLs exhibit a low boundary energy and reactivity due to the high degree of atomic points with a good atomic fit, possibly leading to an improved corrosion resistance of ED-Cu. The SKB wrought Cu showed the largest grain size ($>100\ \mu$m) and greatest uniformity among the Cu materials investigated.

- The differences in microstructure due to pore/interfacial defect density, dislocation density, and/or residual stress, led to an increase in the corrosion rate of the AS-CS-Cu. By comparison, the corrosion behaviour and rate of the HT-CS-Cu were similar to those of the ED-Cu and SKB-Cu indicating the value of the annealing process for the cold sprayed coating. The ED-Cu exhibited marginally increased corrosion resistance in the short term as compared to the SKB-Cu and the HT-CS-Cu.

- CVs and potentiostatic polarizations showed that the electrochemical behaviour of HT-CS-Cu, SKB-Cu and ED-Cu was very similar, while the AS-CS-Cu showed erratic current behavior consistent with a variable surface reactivity.

- Nanoscale STEM-EDX characterization of a cross-section demonstrated the presence of a two-layer Cu_2S film on the surface of the anodically oxidized AS-CS-Cu specimen. In addition, S was detected at a splat boundary tip, indicating that SH^- had diffused into the confined geometry within the surface fractures. The coexistence of S and O on the inter-particle boundaries suggested SH^- had partially converted the oxide impurities known to decorate internal boundaries.

ORCID

Mengnan Guo https://orcid.org/0000-0002-3731-1983
W. Jeffrey Binns https://orcid.org/0000-0003-2472-1251

References

1. D. S. Hall, M. Behazin, W. J. Binns, and P. G. Keech, "An evaluation of corrosion processes affecting copper-coated nuclear waste containers in a deep geological repository." *Prog. Mater Sci.*, **118**, 100766 (2020).
2. F. King, D. S. Hall, and P. G. Keech, "Nature of the near-field environment in a deep geological repository and the implications for the corrosion behaviour of the container." *Corros. Eng. Sci. Technol.*, **52**, 25.
3. A. Hedin, "Long-term safety for KBS-3 repositories at Forsmark and Laxemar-a first evaluation. Main Report of the SR-Can project, Svensk Kärnbränslehantering AB." *Technical Report. SKB-TR-06-09* (2006).
4. "Long-term safety for the final repository for spent nuclear fuel at Forsmark - Main report of the SR-Site project - Volume I, Svensk Kärnbränslehantering AB." *Technical Report. SKB-TR-11-01* (2011).
5. P. G. Keech, M. Behazin, W. J. Binns, and S. Briggs, "An update on the copper corrosion program for the long-term management of used nuclear fuel in Canada." *Mater. Corros.*, **72**, 25 (2020).
6. P. G. Keech, P. Vo, S. Ramamurthy, J. Chen, R. Jacklin, and D. W. Shoesmith, "Design and development of copper coatings for long term storage of used nuclear fuel." *Corros. Eng. Sci. Technol.*, **49**, 425 (2014).
7. C. H. Boyle and S. A. Meguid, "Mechanical performance of integrally bonded copper coatings for the long term disposal of used nuclear fuel." *Nucl. Eng. Des.*, **293**, 403 (2015).
8. H. R. Cornwall, "A summary of ideas on the origin of native copper deposits." *Econ. Geol.*, **51**, 615 (1956).
9. C. C. Patterson, "Native copper, silver, and gold accessible to early metallurgists." *Am. Antiq.*, **36**, 286 (1971).
10. T. J. Bornhorst, J. B. Paces, N. K. Grant, J. D. Obradovich, and N. K. Huber, "Age of native copper mineralization, Keweenaw Peninsula, Michigan." *Econ. Geol.*, **83**, 619 (1988).
11. P. Vo, D. Poirier, J.-G. Legoux, P. G. Keech, D. Doyle, P. Jakupi, and E. Irissou, "Development of cold spray technology for copper coating of carbon steel used fuel container prototypes for CANDU fuel, NWMO." *Technical Report NWMO-TR-2015-29* (2015).
12. J. R. Scully and M. Edwards, "Review of the NWMO copper corrosion allowance." *Technical Report NWMO-TR-2016-11* (2016).
13. T. Standish, J. Chen, R. Jacklin, P. Jakupi, S. Ramamurthy, D. Zagidulin, P. Keech, and D. Shoesmith, "Corrosion of copper-coated steel high level nuclear waste containers under permanent disposal conditions." *Electrochim. Acta*, **211**, 331 (2016).
14. N. Giroud, Y. Tomonaga, P. Wersin, S. Briggs, F. King, T. Vogt, and N. Diomidis, "On the fate of oxygen in a spent fuel emplacement drift in Opalinus Clay." *Appl. Geochem.*, **97**, 270.
15. H. Müller et al., "Implementation of the full-scale emplacement (FE) experiment at the Mont Terri rock laboratory." *Swiss J. Geosci.*, **110**, 287 (2017).
16. F. King, J. Chen, Z. Qin, D. Shoesmith, and C. Lilja, "Sulphide-transport control of the corrosion of copper canisters." *Corros. Eng. Sci. Technol.*, **52**, 210 (2017).
17. J. Chen, Z. Qin, T. Martino, M. Guo, and D. W. Shoesmith, "Copper transport and sulphide sequestration during copper corrosion in anaerobic aqueous sulphide solutions." *Corros. Sci.*, **131**, 245 (2018).
18. M. Guo, J. Chen, T. Martino, C. Lilja, J. A. Johansson, M. Behazin, W. J. Binns, P. G. Keech, J. J. Noël, and D. W. Shoesmith, "The nature of the copper sulfide film grown on copper in aqueous sulfide and chloride solutions." *Mater. Corros.*, **72**, 300 (2020).
19. T. Martino, R. Partovi-Nia, J. Chen, Z. Qin, and D. W. Shoesmith, "Mechanisms of film growth on copper in aqueous solutions containing sulphide and chloride under voltammetric conditions." *Electrochim. Acta*, **127**, 439 (2014).
20. J. Chen, Z. Qin, and D. W. Shoesmith, "Rate controlling reactions for copper corrosion in anaerobic aqueous sulphide solutions." *Corros. Eng. Sci. Technol.*, **46**, 138 (2011).
21. J. Chen, Z. Qin, and D. W. Shoesmith, "Kinetics of corrosion film growth on copper in neutral chloride solutions containing small concentrations of sulfide." *J. Electrochem. Soc.*, **157**, C338.
22. J. Chen, Z. Qin, and D. W. Shoesmith, "Key parameters determining structure and properties of sulphide films formed on copper corroding in anoxic sulphide solutions." *Corros. Eng. Sci. Technol.*, **49**, 415 (2014).
23. S. Briggs, J. McKelvie, P. Keech, B. Sleep, and M. Krol, "Transient modelling of sulphide diffusion under conditions typical of a deep geological repository." *Corros. Eng. Sci. Technol.*, **52**, 200 (2017).
24. S. Briggs, J. McKelvie, B. Sleep, and M. Krol, "Multi-dimensional transport modelling of corrosive agents through a bentonite buffer in a Canadian deep geological repository." *Sci. Total Environ.*, **599**, 348 (2017).
25. T. Martino, J. Chen, Z. Qin, and D. W. Shoesmith, "The kinetics of film growth and their influence on the susceptibility to pitting of copper in aqueous sulphide solutions." *Corros. Eng. Sci. Technol.*, **52**, 61 (2017).
26. T. Martino, J. Smith, J. Chen, Z. Qin, J. J. Noël, and D. W. Shoesmith, "The properties of electrochemically-grown copper sulfide films." *J. Electrochem. Soc.*, **166**, C9 (2019).
27. T. Martino, J. Chen, J. J. Noël, and D. W. Shoesmith, "The effect of anions on the anodic formation of copper sulphide films on copper." *Electrochim. Acta*, **331**, 135319 (2019).
28. J. Chen, Z. Qin, L. Wu, J. J. Noël, and D. W. Shoesmith, "The influence of sulphide transport on the growth and properties of copper sulphide films on copper." *Corros. Sci.*, **87**, 233 (2014).
29. M. Guo, J. Chen, T. Martino, M. Biesinger, J. J. Noël, and D. W. Shoesmith, "The susceptibility of copper to pitting corrosion in borate-buffered aqueous solutions containing chloride and sulfide." *J. Electrochem. Soc.*, **166**, C550 (2019).
30. L. Beaunier, M. Froment, and C. Vignaud, "A kinetical model for the electrochemical grooving of grain boundaries." *Electrochim. Acta*, **25**, 1239 (1980).
31. H. Miyamoto, K. Harada, T. Mimaki, A. Vinogradov, and S. Hashimoto, "Corrosion of ultra-fine grained copper fabricated by equal-channel angular pressing." *Corros. Sci.*, **50**, 1215 (2008).

32. L. Beaunier, "Corrosion of grain boundaries: initiation processes and testing." *J. Phys. Colloq.*, **43**, C6 (1982).

33. B. Yu, J. Tam, W. Li, H. J. Cho, J.-G. Legoux, D. Poirier, J. D. Giallonardo, and U. Erb, "Microstructural and bulk properties evolution of cold-sprayed copper coatings after low temperature annealing." *Materialia.*, **7**, 100356 (2019).

34. W. Li, B. Yu, J. Tam, J. D. Giallonardo, D. Doyle, D. Poirier, J.-G. Legoux, P. Lin, G. Palumbo, and U. Erb, "Microstructural characterization of copper coatings in development for application to used nuclear fuel containers." *J. Nucl. Mater.*, **532**, 152039 (2020).

35. Design, "Production and initial state of the canister, Svensk Kärnbränslehantering AB." *Technical Report SKB-TR-10-14* (2010).

36. G. Palumbo, I. Brooks, K. Tomantschger, P. Lin, K. Aust, N. Nagarajan, and F. Gonzalez, *Method For Preparing Polycrystalline Structures Having Improved Mechanical And Physical Properties*, US009260790B2 (2016).

37. P. Jakupi, P. G. Keech, I. Barker, S. Ramamurthy, R. L. Jacklin, D. W. Shoesmith, and D. E. Moser, "Characterization of commercially cold sprayed copper coatings and determination of the effects of impacting copper powder velocities." *J. Nucl. Mater.*, **466**, 1 (2015).

38. "Long-term safety for the final repository for spent nuclear fuel at Forsmark Main report of the SR-Site project - Volume II, Svensk Kärnbränslehantering AB." *Technical Report. SKB-TR-11-01* (2011).

39. "Long-term safety for the final repository for spent nuclear fuel at Forsmark Main report of the SR-Site project Volume III, Svensk Kärnbränslehantering AB." *Technical Report. SKB-TR-11-01* (2011).

40. K. D. Ralston and N. Birbilis, "Effect of grain size on corrosion: a review." *Corrosion*, **66**, 075005 (2010).

41. K. D. Ralston, N. Birbilis, and C. H. J. Davies, "Revealing the relationship between grain size and corrosion rate of metals." *Scr. Mater.*, **63**, 1201 (2010).

42. D. A. Porter and K. E. Easterling, *Phase Transformations In Metals And Alloys (Revised Reprint)* (CRC press, Boca Raton) (2009).

43. W. D. Callister Jr. and D. G. Rethwisch, *Callister's Materials Science And Engineering* (Wiley, New York, NY) (2020).

44. J. Tam, W. Li, B. Yu, D. Poirier, J.-G. Legoux, P. Lin, G. Palumbo, J. D. Giallonardo, and U. Erb, "Reducing complex microstructural heterogeneity in electrodeposited and cold sprayed copper coating junctions." *Surf. Coat. Technol.*, **404**, 126479 (2020).

45. W. Li, "Microstructural characterization of copper coatings on nuclear waste containers for the long-term disposal of Canada's used nuclear fuel." *PhD Thesis*, University of Toronto (2018), http://hdl.handle.net/1807/91707.

46. A. Dobkowska, M. Castillo, J. P. Turnbull, S. Ramamurthy, D. Zagidulin, D. Moser, M. Behazin, P. Keech, D. W. Shoesmith, and J. J. Noël, "A comparison of the corrosion behaviour of copper materials in dilute nitric acid." *Corros. Sci.*, 109778 (2021).

47. T. Standish, "Galvanic corrosion of copper-coated carbon steel for used nuclear fuel containers." *PhD thesis*, The University of Western Ontario (2019), Western University, https://ir.lib.uwo.ca/etd/6705.

48. R. Wu, J. Hagström, and R. Sandström, "Grain boundary sliding in phosphorus alloyed oxygen-free copper under creep - Google Search, Svensk Kärnbränslehantering AB." *Report.* (2015).

49. H. C. M. Andersson-Östling, J. Hagström, and M. Danielsson, "Phosphorus in copper intended for spent nuclear fuel disposal, Svensk Kärnbränslehantering AB." *Report* (2018).

50. C. Lee and J. Kim, "Microstructure of kinetic spray coatings: a review." *J. Therm. Spray Technol.*, **24**, 592 (2015).

51. D. G. Brandon, "The structure of high-angle grain boundaries." *Acta Metall.*, **14**, 1479 (1966).

52. Y. Ghaffari, K. Daub, R. C. Newman, and S. Y. Persaud, "Internal oxidation of Ag-xIn alloys at low homologous temperature." *Corros. Sci.*, **175**, 108869 (2020).

53. V. Randle, "The coincidence site lattice and the 'sigma enigma." *Mater. Charact.*, **47**, 411 (2001).

54. D. S. Hall and P. G. Keech, "An overview of the Canadian corrosion program for the long-term management of nuclear waste." *Corros. Eng. Sci. Technol.*, **52**, 2 (2017).

55. J. Chen, Z. Qin, T. Martino, and D. W. Shoesmith, "Effect of chloride on Cu corrosion in anaerobic sulphide solutions." *Corros. Eng. Sci. Technol.*, **52**, 40 (2017).

56. M. Guo, J. Chen, C. Lilja, V. Dehnavi, M. Behazin, J. J. Noël, and D. W. Shoesmith, "The anodic formation of sulphide and oxide films on copper in borate-buffered aqueous chloride solutions containing sulphide." *Electrochim. Acta*, **362**, 137087 (2020).

57. T. L. Martino, "Electrochemical and corrosion examination of copper under deep geologic conditions for the application of nuclear waste containers." *PhD Thesis*, The University of Western Ontario (2018), https://ir.lib.uwo.ca/etd/5227.

58. M. Guo, *The Electrochemical And Corrosion Study Of Copper For Nuclear Waste Containers Under Deep Geological Disposal Conditions*, The University of Western Ontario (2020), https://ir.lib.uwo.ca/etd/7371.

59. J. Smith, Z. Qin, F. King, L. Werme, and D. W. Shoesmith, "Sulfide film formation on copper under electrochemical and natural corrosion conditions." *Corrosion*, **63**, 135 (2007).

60. I. Puigdomenech and C. Taxén, "Thermodynamic data for copper. Implications for the corrosion of copper under repository conditions, Svensk Kärnbränslehantering AB." *Technical Report SKB-TR-00-13* (2000).

61. H.-P. Hermansson, "Copper thermodynamics in the repository environment up to 130 °C, swedish radiation safety authority." *Report SSM-2010-09* (2010).

62. G. W. Luther, S. M. Theberge, T. F. Rozan, D. Rickard, C. C. Rowlands, and A. Oldroyd, "Aqueous copper sulfide clusters as intermediates during copper sulfide formation." *Environ. Sci. Technol.*, **36**, 394 (2002).

63. A. J. Bard, L. R. Faulkner, J. Leddy, and C. G. Zoski, *Electrochemical Methods: Fundamentals And Applications* (Wiley, New York, NY) (1980).

64. V. S. Bagotsky, *Fundamentals of electrochemistry* (Wiley, New York, NY) (2005).

65. T. Kosec, Z. Qin, J. Chen, A. Legat, and D. W. Shoesmith, "Copper corrosion in bentonite/saline groundwater solution: Effects of solution and bentonite chemistry." *Corros. Sci.*, **90**, 248 (2015).